Investigation on Suitability of Ripple Correlation Control Based MPPT for One Cycle Controlled Single Phase Two Stage Grid Connected PV Systems

Raghavendra Bandaru, Sreeraj E. S., *Member, IEEE*, and Puneet Kumar Goel

***Abstract*—This paper proposes a single-phase two-stage grid-tied photovoltaic (PV) system employing ripple correlation control (RCC) for performing maximum power point tracking (MPPT) and one-cycle control (OCC) for operating the common-ground transformerless inverter (CGI). It is well known that RCC-based MPPT is quite effective for single-phase single-stage systems because of the presence of 100 Hz ripple in the PV array capacitor. In the case of two-stage systems, the 100 Hz ripple is predominantly present on the DC-link side of the inverter. However, a small component of this ripple is back-propagated to the capacitor connected in parallel with the PV array. This is the feature that has been exploited to implement RCC-based MPPT in the single-phase two-stage system, and its performance in comparison with conventional MPPT techniques is investigated in this paper. The OCC technique ensures effective grid synchronization and current regulation without requiring a phase-locked loop (PLL). In addition, the CGI employed for power conversion ensures a fixed common-mode voltage, which eradicates leakage currents. Furthermore, the modulation strategy employed for the CGI ensures that only two switches are operating at the switching frequency, while the remaining two are operating at the power frequency, lowering the switching loss. The proposed configuration combines all the aforementioned features, ensuring a reduction in overall system cost and complexity. The performance of the proposed system is analyzed through simulations using MATLAB/Simulink, and the experimental setup of the controller is implemented on a TMS320F28335 digital signal processor and evaluated using hardware-in-the-loop testing. The proposed system is further experimentally validated using an experimental test bench implemented in the laboratory.**

Link to graphical and video abstracts, and to code:
https://latamt.ieeer9.org/index.php/transactions/article/view/10850

***Index Terms*—Ripple Correlation Control MPPT, Common Ground Transformerless Inverter, One Cycle Control.**

I. Introduction

SOLAR photovoltaic (PV) systems have gained increasing attention due to their environmentally friendly nature, modularity, low maintenance requirements, and suitability for both grid-connected and stand-alone applications. Residential consumers are increasingly encouraged by government policies and incentives to install rooftop solar panels that can be integrated with the grid [1], [2], [3]. Since many residential consumers are supplied through single-phase connections, it is essential to have single-phase grid-connected PV systems rated below 2 kW, which can also provide grid support at the distribution level [4]. These systems become practically feasible only when the complexity and cost associated with the control architecture are minimized. The single-phase PV system can be classified as either single-stage or two-stage, depending on the power conversion stages. In a single-stage system, the power conversion can be carried out using only one power conversion stage, typically through a single inverter. Therefore, the inverter control handles maximum power point tracking (MPPT), grid synchronization, and reactive power compensation using appropriate control techniques [5]. Although a single-stage system offers simplicity and reduced component count, it suffers from control complexity, limited voltage regulation, and component stress. Moreover, it generally requires a more PV modules connected in series to meet the DC link voltage requirements.

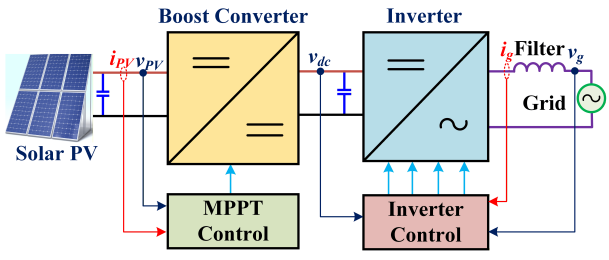

Fig. 1. Schematic representation of the single-phase two-stage grid-connected PV system.

These aforementioned problems are addressed by a two-stage system [12], which includes a front-end DC-side converter followed by an inverter stage as shown in Fig.1. The DC-side converter boosts the maximum voltage tracked by MPPT to the desired DC-link voltage, providing the flexibility in control and stability for the system. A wide range of MPPT

The associate editor coordinating the review of this manuscript and approving it for publication was Guillermo Valencia-Palomo (*Corresponding author: Sreeraj E. S.).*

The authors are very thankful to the Goa Energy Development Agency(GEDA), Govt. of Goa, for funding this project under grant number 1/450/22-23/GEDA/110.

R. Bandaru, and Sreeraj E. S. are with the Department of Electrical and Electronics Engineering, National Institute of Technology Goa, Goa 403703, India (e-mails: raghavendra@nitgoa.ac.in, and sreeraj@nitgoa.ac.in).

P. K. Goel is the chairman of Manipur State Power Company Limited, Manipur, India (e-mail: cs-manipur@nic.in).

TABLE I
COMPARISON OF DIFFERENT MPPT TECHNIQUES

MPPT	Response time (ms)	Convergence speed	Efficiency	Cost	Reliability	Complexity	MPP oscillations
P&O [6]	60-100 ms	Fast	98.1%	Low	High	Low	Medium
INC [6]	20-70 ms	Medium	99.2%	Moderate	High	Moderate	Medium
PSO [7]	300-350 ms	Low	99.5%	High	Moderate	High	Low
Hybrid [8]	150-200 ms	Medium	97.1%	High	Moderate	High	Low
FLC [9]	250-400 ms	Low	99.6%	Moderate	High	High	Low
ANN [7]	250-450 ms	Low	99.7%	High	Moderate	Very high	Low
RCC [10], [11]	80-110 ms	Fast	99.8%	Moderate	High	Moderate	Low

techniques for solar PV systems have been reported in the literature, which are summarized in Table I. These methodologies include conventional perturb and observe (P&O) and incremental conductance, hill-climbing, hybrid approaches, meta-heuristic optimization, artificial intelligence and fuzzy logic-based methods, and ripple correlation control (RCC) [6], [13], [14], [8], [9], [7]. Most of the aforementioned techniques rely on introducing artificial perturbations to maintain the operating point of the PV array near the maximum power point (MPP). The P&O method is a commonly used MPPT technique for its simplicity and fast convergence, but it may lead to oscillations and loss of tracking near the MPP under rapid irradiance variations [15]. In contrast, the RCC-based MPPT method presented in [10], [11], [16], [17] exploits the inherent ripple components of the system to track the MPP. This technique was originally proposed for systems given in [10], [11] in which the switching-frequency ripple present in PV voltage and current is used to track the MPP, rather than relying on external perturbations. However, in single-phase single-stage systems, the capacitor connected across the PV array inherently contains a 100 Hz ripple, which facilitates the implementation of RCC-based MPPT using a low-bandwidth controller, and its effectiveness has been well demonstrated in [16], [17]. In single-phase two-stage systems, the 100 Hz ripple is predominantly present on the DC-link side; however, a small component is reflected back to the capacitor connected in parallel with the PV array, and its impact on MPPT effectiveness has not been thoroughly investigated. This work explores the use of this ripple via ripple correlation control (RCC) MPPT and evaluates its performance in comparison with conventional MPPT methods.

TABLE II
COMPARISON OF TRANSFORMERLESS INVERTER TOPOLOGIES

Inverter topology	Components S	D	C	L	Switching frequency	Leakage current	Reactive power support
H5 [18], [19]	5	1	2	0	20 kHz	Less	No
H6 [18], [19]	6	2	2	0	20 kHz	Less	No
HERIC [18], [19]	6	2	1	0	10 kHz	Less	Yes
Type-I [20]	4	1	2	0	50 kHz	Zero	Yes
Type-II [20]	4	1	2	0	50 kHz	Zero	Yes
Type-III [20]	4	0	2	0	16 kHz	Zero	Yes

S = Switches; D = Diodes; C = Capacitors; L = Inductors.

Among the various single-phase inverter topologies reviewed and summarized in Table II, common-ground transformerless inverter (CGI) configurations are gaining popularity due to their compact design, simplified structure, and constant common-mode voltage performance [18], [19], [21], [22], [23], [20]. In [20], a family of CGIs was proposed for single-phase operation, and the Type-I CGI is adopted in this work due to its lower component count and uniform semiconductor voltage stress. Here, a basic unipolar modulation (UPM) with three switching states used for control the inverter switches.

However, this modulation technique impacts the flying capacitor size and causes excessive stress on certain active switches. To address this, the modulation strategy employed for the inverter ensures that only two of the four switches are operate at the switching frequency, while the other two switched at the power frequency, thereby reducing reliance on high-frequency switching devices.

Various control strategies have been discussed in the literature to enable effective grid interfacing of single-phase inverters, as detailed in [5], [12] and [24], [25], [26], [27], [28], [29], [30], [31], [32], [33]. The single-phase inverter control methods given in [24], [25], [26], [27] designed for grid interfacing employ a phase-locked loop (PLL) to achieve synchronisation with grid voltage, which increases computational complexity due to the continuous tracking and processing involved. Moreover, implementing the PLL imposes a considerable computational burden on the digital signal processor (DSP). Systems based on one-cycle control (OCC) proposed in [28], [29] eliminate the need for a PLL in their operation, thereby simplifying the control process and reducing computational demands. Among the OCC-based schemes reported, an approach is proposed in [29], which utilizes only two sensors and eliminates the need for a grid voltage sensor. Consequently, the control scheme is simplified and more suitable for small-scale distributed PV installations with single-phase grid connection. The OCC inverter has also demonstrated superior effectiveness in passive islanding detection compared to other control methods [30]. There is still an existing research gap regarding the implementation of the OCC technique in two-stage inverter systems, indicating the need for further investigation in this area. A comparative analysis of inverter control has been reported for three-phase PV-grid connection systems [34], [35], [36]; however, similar comprehensive studies for single-phase PV-grid connection systems are rarely found. This drives the need for a comparative assessment of various control methodologies applied

to single-phase inverters.

The major contributions of this work can be summarized as follows:

The RCC MPPT is effectively used for a single-stage system, where the PV array directly contains the ripple at twice the line frequency (100 Hz in 50-Hz system). However, the two-stage system also has this ripple back-propagated with a lower magnitude, and this is investigated for the first time. In order to understand the amount of this ripple back-propagated from the DC-link capacitor to the PV array, an average model is developed, providing a theoretical basis for understanding the operational limits of the RCC algorithm. In addition, the proposed RCC implementation employs low-pass filters and avoids derivative-based computations, thereby reducing sensitivity to measurement noise and ensuring reliable MPP tracking performance under noisy operating conditions. Furthermore, the proposed system integrates several features for the first time, including PLL-less grid synchronization through OCC control, constant common-mode voltage operation using the Type-I common-ground inverter, and a modulation strategy that reduces the requirement for high-frequency switching devices. These features collectively contribute to lower system cost and complexity while maintaining effective MPPT and grid-integration performance.

The paper is organized as follows. Section II discusses the system configuration and principal operation of the proposed system. Section III presents the control algorithms of the system. Design considerations are given in section IV. Section V presents simulation studies and experimental validation of the proposed RCC-based MPPT using an experimental test bench, followed by a performance comparison of the considered control strategies using hardware-in-the-loop (HIL) testing. Finally, Section VI presents the conclusions.

II. Proposed System Configuration and Principle of Operation

Fig. 2 illustrates the two-stage grid-connected PV system topology, comprising a PV array, boost converter, and single-phase inverter. The RCC MPPT-based boost converter maximizes power extraction from the PV array and feeds it to the inverter. This inverter operates using sinusoidal PWM and OCC techniques to achieve synchronisation and inject the converted AC power into the grid via an LC filter. The comparative study of various single-phase transformerless inverter topologies is given in Table II and Table IV. The Type-I inverter [20] is selected in this work because of its reduced component count, zero leakage current, reactive power support capability, high efficiency, and suitable switching frequency compared with other transformerless inverter topologies. Conventional configurations such as H5, H6, and HERIC limit the voltage stress on the switches to $v_{\rm dc}$; however, they require five to six active switches. In contrast, the Type-I topology achieves the same voltage-stress limit using only four active switches and one diode, reducing semiconductor count and gate-drive requirements. Moreover, compared with other common-ground inverter topologies, such as Type-II and Type-III, which impose a higher voltage stress of $2v_{\rm dc}$ on certain switches, the Type-I topology requires lower device voltage ratings and can reduce the associated semiconductor losses. The schematic of Type-1 inverter as depicted in Fig. 3(a), comprises four active switches (S_1–S_4), a diode (D), flying capacitor (C_{fc}). Inverter switches operate such that the DC bus supplies output for positive power half-cycle, while the flying capacitor delivers power for the negative half-cycle. Fig. 3(b) shows the switching logic of the CGI, where two of the four switches operate at the switching frequency and the other two operate at the power frequency. This configuration minimizes the switching loss, reduce the count of high switching frequency devices and supports the grid's reactive power requirement. With this switching logic switches S_1 and S_2 operate at switching frequency while switches S_3 and S_4 function at power frequency. The overview of the different switching states of CGI is described in Table III and Table V.

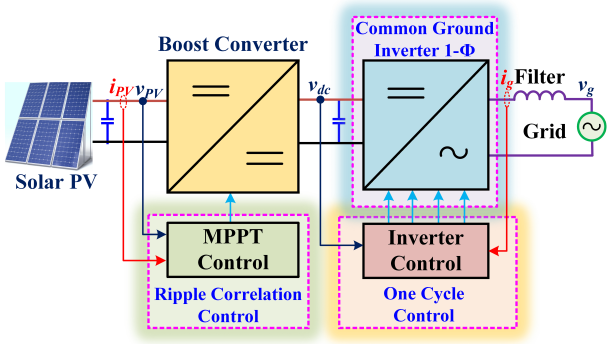

Fig. 2. Architecture of the two-stage PV system under study.

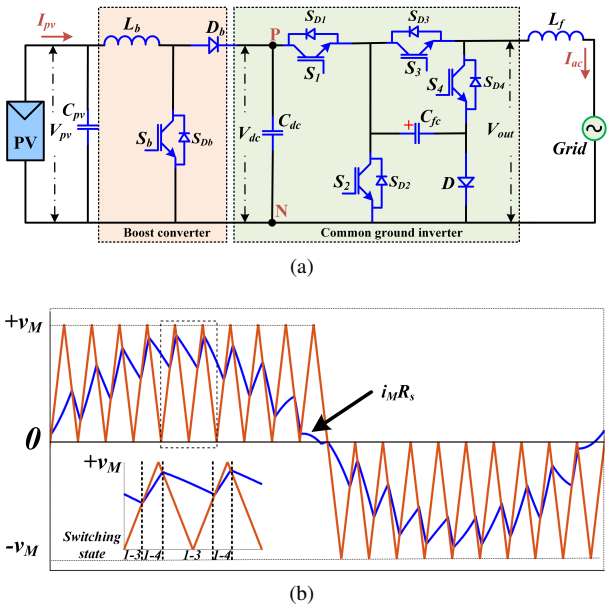

Fig. 3. (a) Schematic of the two-stage PV system under study, (b) Switching logic for CGI.

A. Operating Modes of CGI

The equivalent circuits of CG inverter in various operating modes are given in Fig. 4 and are described as follows:

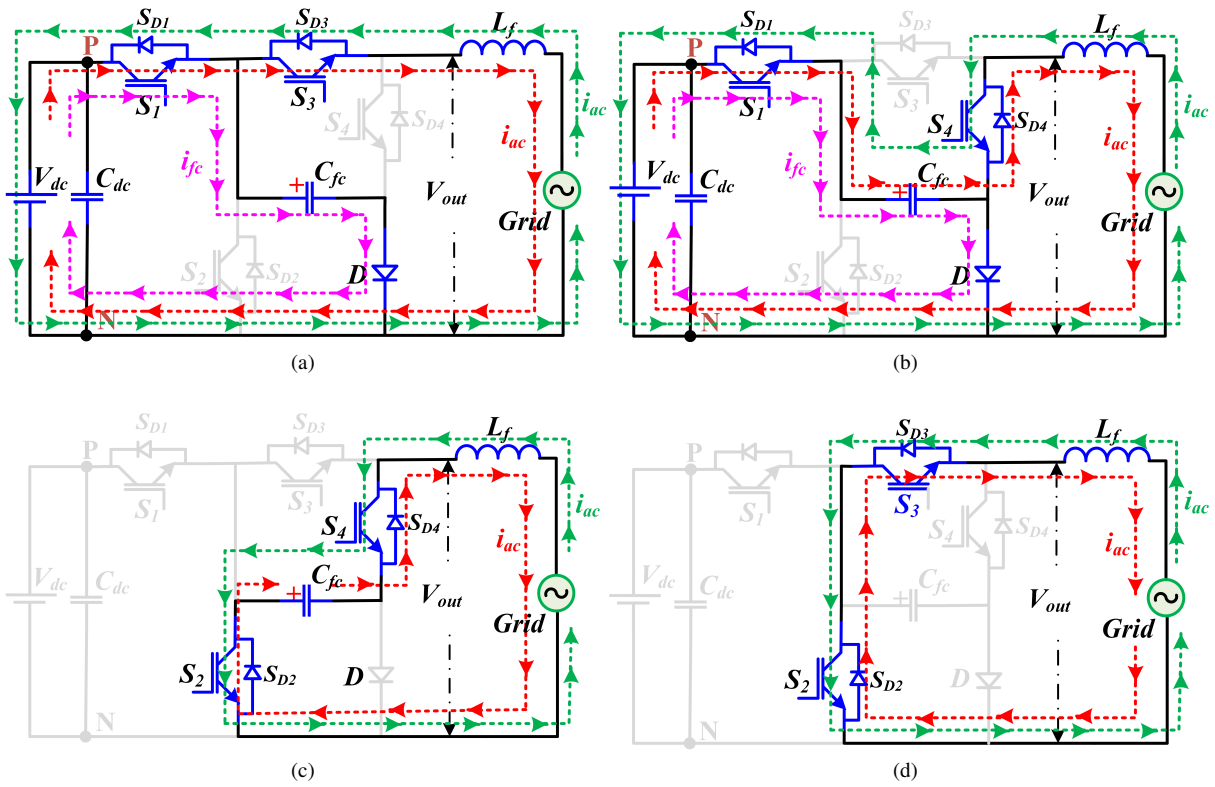

Fig. 4. Equivalent circuits in various operating modes of CGI. (a) Mode-I [S_1,S_3 ON], (b) Mode-I [S_1,S_4 ON], (c) Mode-II [S_2,S_4 ON], and (d) Mode-II [S_2,S_3 ON].

TABLE III
SWITCHING STATES OF THE CGI AND THEIR CORRESPONDING OUTPUT VOLTAGES

Switching states(SS)	S_1	S_2	S_3	S_4	v_{out}
Switching state-1	1	0	1	0	$+v_{dc}$
Switching state-2	1	0	0	1	0
Switching state-3	0	1	0	1	$-v_{dc}$
Switching state-4	0	1	1	0	0

1) Mode-I: In this operating mode, switches S_1 and D are kept ON throughout the positive half-cycle, facilitating the pre-charging of the C_{fc} in anticipation of the negative cycle. Switch S_2 remains closed for the entire positive period, further supporting the charging process of the C_{fc}. Switches S_3 and S_4 operate at high switching frequency to generate positive and zero voltage levels at the filter during each switching event.

Positive active: In this state, the switches S_1 and S_3 are ON, resulting in a positive voltage ($+v_{\text{dc}}$) being established at the filter output, and flying capacitor charges through the loop: $v_{\text{dc}} \rightarrow S_1 \rightarrow C_{fc} \rightarrow D \rightarrow v_{\text{dc}}$, as illustrated in Fig. 4(a). Therefore, the voltage at filter output is given as:

$$v_{out} = v_{fc} = +v_{dc} \tag{1}$$

During this state, the positive current path is $v_{\text{dc}} \rightarrow S_1 \rightarrow S_3 \rightarrow L_{\text{f}} \rightarrow$ grid, while the return (negative) current path is grid $\rightarrow L_{\text{f}} \rightarrow S_{D3} \rightarrow S_{D1} \rightarrow v_{\text{dc}}$.

Positive zero: Following the positive active state, switches S_1 and S_4 are turned ON to produce a zero voltage at the filter. In this stage, the C_{fc} charges through $v_{dc} \rightarrow S_1 \rightarrow C_{fc} \rightarrow S_{D4} \rightarrow L_f \rightarrow$ grid, and for negative current, it is grid $\rightarrow L_f \rightarrow S_4 \rightarrow C_{fc} \rightarrow S_{D1} \rightarrow v_{dc}$, as illustrated in Fig. 4(b). The C_{fc} is assumed sufficiently large to maintain nearly constant voltage across switching cycles, such that $v_{fc} \approx v_{dc}$. Therefore, the equivalent voltage before the filter inductor is given as:

$$v_{out} = v_{dc} - v_{fc} \approx 0. \tag{2}$$

2) Mode-II: In this mode the switch S_1 OFF and switch S_2 remains ON for the whole negative cycle. Switches S_3 and S_4 operate at switching frequency to generate negative and zero voltage levels at the filter during each switching event.

Negative active: In the negative active state, switches S_2 and S_4 are turned ON, allowing the energy stored in the capacitor C_{fc} to supply voltage, which results in a negative voltage (-v_{dc}) at the filter, as depicted in Fig. 4(c). When S_2 is ON, diode D becomes reverse-biased automatically. In this condition, the positive current path follows: $C_{fc} \rightarrow S_{D4} \rightarrow L_f \rightarrow$ grid $\rightarrow S_{D2} \rightarrow C_{fc}$, while the return (negative) current path is: Grid $\rightarrow L_f \rightarrow S_4 \rightarrow C_{fc} \rightarrow S_2 \rightarrow$ grid. The equivalent voltage before the filter inductor is given as:

$$v_{out} = -v_{dc} \tag{3}$$

Negative zero: This mode represents the freewheeling operation where switches S_2 and S_3 are ON, producing a zero voltage at the filter input. In this condition, diode D

TABLE IV
VOLTAGE, CURRENT STRESS AND EFFICIENCY ANALYSIS OF COMMON GROUND AND TRANSFORMERLESS TOPOLOGIES [20]

Topologies	Stress	Semiconductor Devices							Efficiency
		S_1	S_2	S_3	S_4	S_5	S_6	Diode	
H5 [18], [19]	Voltage Stress	$+v_{\rm dc}$	$+v_{\rm dc}$	$+v_{\rm dc}$	$+v_{\rm dc}$	$+v_{\rm dc}$	–	–	98.5%
	Current Stress	$I_{\rm o,m}$	$I_{\rm o,m}$	$I_{\rm o,m}$	$I_{\rm o,m}$	$I_{\rm o,m}$	–	–	
H6 [18], [19]	Voltage Stress	$+v_{\rm dc}$	$+v_{\rm dc}$	$+v_{\rm dc}$	$+v_{\rm dc}$	$+v_{\rm dc}$	$+v_{\rm dc}$	–	97.4%
	Current Stress	$I_{\rm o,m}$	$I_{\rm o,m}$	$I_{\rm o,m}$	$I_{\rm o,m}$	$I_{\rm o,m}$	$I_{\rm o,m}$	–	
HERIC [18], [19]	Voltage Stress	$+v_{\rm dc}$	$+v_{\rm dc}$	$+v_{\rm dc}$	$+v_{\rm dc}$	$+v_{\rm dc}$	$+v_{\rm dc}$	–	97%
	Current Stress	$I_{\rm o,m}$	$I_{\rm o,m}$	$I_{\rm o,m}$	$I_{\rm o,m}$	$I_{\rm o,m}$	$I_{\rm o,m}$	–	
Type-I[20]	Voltage Stress	$+v_{\rm dc}$	$+v_{\rm dc}$	$+v_{\rm dc}$	$+v_{\rm dc}$	–	–	$v_{\rm dc}$	99.2%
	Current Stress	$\approx \left[\frac{0.5D_m}{1-D_m}\frac{2+\delta}{1+\delta}\right] I_{\rm o,m}$	$\approx I_{\rm o,m}$	$\approx I_{\rm o,m}$	$\approx I_{\rm o,m}$	–	–	$\approx \left[\frac{0.5D_m}{1-D_m}\frac{2+\delta}{1+\delta}+1\right] I_{\rm o,m}$	
Type-II[20]	Voltage Stress	$+v_{\rm dc}$	$+v_{\rm dc}$	$+2v_{\rm dc}$	$+v_{\rm dc}$	–	–	–	99.2%
	Current Stress	$\approx \left[\frac{0.5D_m}{1-D_m}\frac{2+\delta}{1+\delta}\right] I_{\rm o,m}$	$\approx I_{\rm o,m}$	$\approx I_{\rm o,m}$	$\approx I_{\rm o,m}$	–	–	$\approx \left[\frac{0.5D_m}{1-D_m}\frac{2+\delta}{1+\delta}+1\right] I_{\rm o,m}$	
Type-III[20]	Voltage Stress	$\pm v_{\rm dc}$	$+2v_{\rm dc}$	$+2v_{\rm dc}$	$\pm v_{\rm dc}$	–	–	N/A	97.6%
	Current Stress	$\approx \left[\frac{0.5D_m}{1-D_m}\frac{2+\delta}{1+\delta}\right] I_{\rm o,m}$	$\approx I_{\rm o,m}$	$\approx I_{\rm o,m}$	$\approx \left[\frac{0.5D_m}{1-D_m}\frac{2+\delta}{1+\delta}+1\right] I_{\rm o,m}$	–	–	N/A	

$v_{\rm dc}$: DC-link voltage; D_m: Maximum duty cycle; $I_{\rm o,m}$: Maximum amplitude of load current; δ: $C_{\rm fc}/C_{\rm dc}$.

TABLE V
OPERATING QUADRANTS CORRESPONDING TO THE SWITCHING STATES OF THE CGI

Quadrant	Switching States	V_{ac}, i_{ac}
I	SS-1, SS-4	+, +
II	SS-3, SS-2	-, +
III	SS-3, SS-2	-, -
IV	SS-1, SS-4	+, -

becomes reverse-biased, effectively isolating both the DC bus and the flying capacitor, as shown in Fig. 4(d). During this state, bidirectional current paths are established through S_2 and S_{D3}, as well as through S_3 and S_{D3}. This operation allows the circuit to maintain zero voltage across the filter while isolating the energy storage elements, facilitating smooth freewheeling current flow. The described modes of operation, repeats periodically in every power cycle, producing unipolar voltage at the filter input. This voltage is subsequently filtered to deliver a smooth sinusoidal voltage and current to the grid.

Compared to the UPM used in [20], the modulation adopted in this work effectively lowers the need for high-frequency switching devices, which in turn reduces both the overall cost and switching losses.

III. CONTROL ALGORITHM FOR THE PROPOSED SYSTEM

A. RCC MPPT

RCC-based MPPT in two-stage PV grid systems uses the natural voltage and current (or power) ripples generated by the switching actions of the DC-DC converter. By correlating these ripples with the converter's switching signals, RCC dynamically determines the optimal duty cycle to maximize power extraction without introducing external disturbances. Fig. 5 illustrates that the MPP is achieved when the product of the ripple components in PV voltage and PV power over one switching frequency cycle equals zero. The sign of this product, whether positive or negative, indicates the direction of the operating point relative to the MPP either to the left or the right. Furthermore, the average value of this product directly correlates with the operating point deviation from the MPP, as mathematically expressed below.

Consider a periodic quantity $x(t)$ with period T. Its average component over one complete period is denoted by $\overline{x}(t)$, while $\widetilde{x}(t)$ represents the corresponding ripple component and is expressed as:

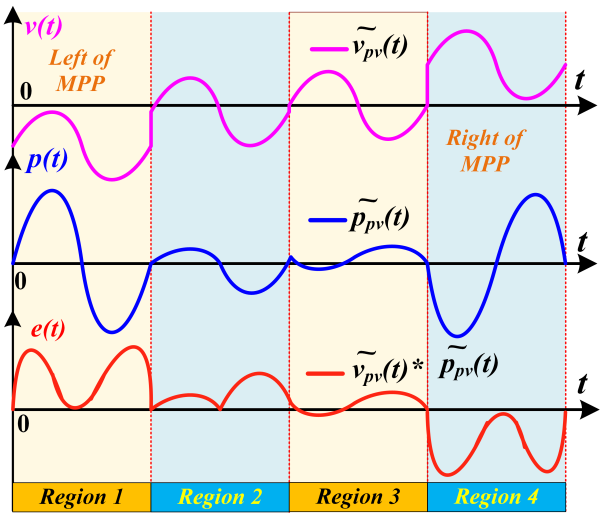

Fig. 5. Ripple in PV voltage and power.

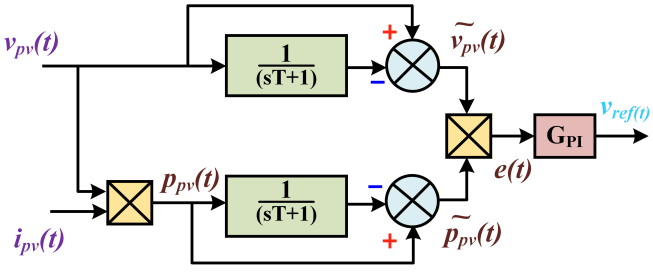

Fig. 6. Schematic of RCC MPPT technique.

$$\tilde{x}(t) = x(t) - \overline{x}(t) \tag{4}$$

To extract the 100 Hz ripple component $\tilde{x}(t)$, the moving average $\overline{x}(t)$ must first be isolated from the instantaneous signal $x(t)$ using a low-pass filter (LPF). To ensure maximum attenuation of the 100 Hz double-line-frequency ripple while maintaining an acceptable dynamic tracking response, the LPF cut-off frequency (f_c) is strictly constrained to $f_c \ll 100$ Hz. In this system, f_c is tuned to 63.66 Hz, resulting in a filter time constant of $\tau = 1/(2\pi f_c) \approx 2.5$ ms. This tuning effectively suppresses the 100 Hz component in the averaged signal, allowing the subtraction block to accurately isolate the AC ripple for the control loop. The product of PV voltage and current, representing instantaneous PV power and is expressed as follows.

$$p_{pv}(t) = v_{pv}(t) i_{pv}(t) \tag{5}$$

Using equations (4) and (5, $\widetilde{p}_{pv}(t)\,\widetilde{v}_{pv}(t)$ can be derived as

$$\widetilde{p}_{pv}(t)\,\widetilde{v}_{pv}(t) = \widetilde{v}^2_{pv}(t)\left(\frac{d_{p_{pv}}(t)}{d_{v_{pv}}(t)}\right) + \widetilde{v}^2_{pv}(t)\,\widetilde{i}^2_{pv}(t) \tag{6}$$

The average value of $\tilde{v}^2_{pv}(t)\,\tilde{i}^2_{pv}(t)$ over one cycle is zero, indicating that the error voltage $\tilde{e}(t)$, which is defined as $\tilde{p}_{pv}(t)\,\tilde{v}_{pv}(t)$, is directly proportional to the ratio $\dfrac{dp_{pv}(t)}{dv_{pv}(t)}$. Consequently, this error signal, being proportional to changes in PV power, reflects the distance of the operating point from the MPP. As reported in [17] and shown in Fig. 6, the RCC control scheme employs two low-pass filters, a multiplier, and two adders to extract the ripple voltage and ripple power components from the measured PV voltage and current. These ripple components are multiplied to generate the error signal $\tilde{e}(t)$, which is then passed to a PI controller. The PI controller outputs the reference PV voltage that serves as the control input to the PWM controller responsible for generating switching pulses for the boost converter. The two-stage configuration enables RCC to manage the slower dynamics of the DC-DC converter stage, while the inverter stage handles the faster power conversion dynamics. This separation results in improved system stability, enhanced efficiency, and robust MPPT tracking performance under varying environmental conditions. Consequently, the RCC effectively regulates the overall PV system by coordinating these two stages to optimize power extraction and maintain steady grid integration.

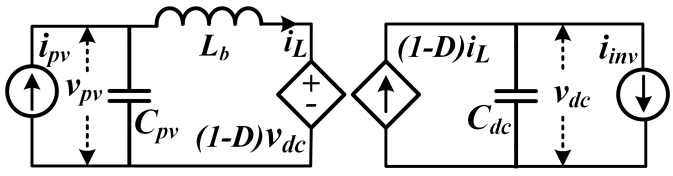

Fig. 7. Averaged model of the two stage system.

B. Ripple back Propagated to the PV Array

The RCC algorithm discussed in the previous section relies on the ripple at twice the line frequency (100 Hz in 50 Hz system) that propagates from the DC-link to the PV terminals through the boost converter. The primary source of this ripple is the presence of ripple at twice the line frequency in the single-phase power fed to the grid, and its magnitude depends on the load current and the size of the DC-link capacitor [24]. As the considered ripple is not a high-frequency ripple, a simple average model shown in Fig. 7 is used to determine the amount of ripple back-propagated to the PV array. In this model, the PV array is modeled as a constant current source, i_{pv}, neglecting the small amount of ripple present in the PV power. The average voltage across the boost-converter switch is modeled as a voltage source, which is a function of the duty ratio (D) and v_{dc}. Similarly, the average model of the inverter output current is a function of D and the inductor current (i_L). Based on this model, the transfer function relating the PV-side ripple voltage to the DC-link ripple voltage is given by

$$\frac{v_{pv}(s)}{v_{dc}(s)} = \frac{1-D}{1 + L_b C_{pv} s^2} \tag{7}$$

where D is the boost-converter duty ratio, L_b is the boost inductance, and C_{pv} is the PV-side capacitance. At the double-line frequency, f_r = 100 Hz, the magnitude of the ripple propagation ratio is therefore

$$\left|\frac{v_{pv}}{v_{dc}}\right| = \frac{1-D}{|1 - L_b C_{pv}(2\pi f_r)^2|} \tag{8}$$

for the converter parameters given in Table VI, the term $L_b C_{pv}(2\pi f_r)^2$ is much smaller than unity. Hence, at 100 Hz, 8 can be approximated as

$$\left|\frac{v_{pv}}{v_{dc}}\right| \approx (1-D). \tag{9}$$

Equation 9 shows that the low-frequency ripple transfer from the dc-link to the PV terminal is primarily governed by the boost-converter conversion ratio.

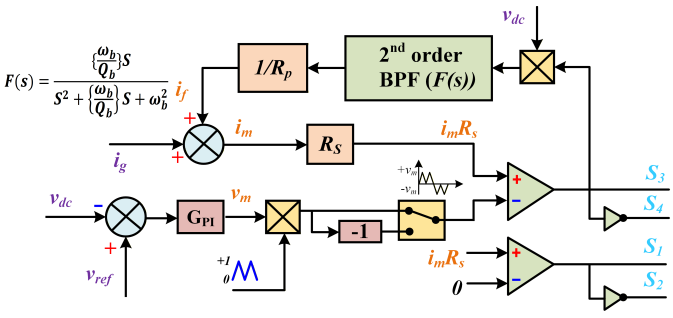

Fig. 8. Schematic of sensor-less One-Cycle-Control.

C. Sensor-less One-Cycle Control(OCC)

The control scheme of the grid-voltage sensorless one-cycle controller(OCC), detailed in [29] and shown in Fig. 8, relies on comparing the DC-link voltage V_{dc} to reference voltage V_{ref}. The resulting error signal is processed by a proportional-integral (PI) controller, producing the modulating voltage V_M.

This modulating voltage is then multiplied by a triangular carrier signal with a magnitude of ± 1 and a switching period T_s to generate a carrier waveform of magnitude V_M. Subsequently, the carrier waveform is compared with the product $i_m R_S$, where R_S is the current sensor gain to generate the switching pulses. This current i_m is the sum of the grid current i_g and a fictitious current component i_f. The i_f is proportional to the fundamental inverter voltage component v_{I1}. The v_{I1} gets estimated using a second-order band-pass filter on the inverter switching function, followed by saturation. The signal i_m is expressed as

$$i_m = i_g + i_f = i_g + \frac{v_{I1}}{R_p} \tag{10}$$

when $i_m R_s$ exceeds the carrier signal S_1, switches S_1 and S_3 are activated, producing an inverter output of v_{dc}. Conversely, when $i_m R_s$ is below the carrier signal S_2, switches S_2 and S_4 are activated, resulting in an inverter output of $-v_{dc}$. The average value of the inverter output voltage in one switching cycle is given as follows,

$$v_I = v_{dc}\left(\frac{V_m + i_m R_S}{2V_M} - \frac{V_m - i_m R_S}{2V_M}\right) = i_m R_S\left(\frac{v_{dc}}{V_M}\right) \tag{11}$$

where R_s is the current sensor gain and the parameter R_p must be selected to fulfill the stability conditions outlined in [29] while ensuring that the system delivers its rated power to the grid.

IV. Design Considerations

A. PV Capacitor (C_{pv}):

The fluctuation in PV voltage caused by the dynamic behavior of the PV solar panel resembles capacitance. To minimize voltage ripple and shield the PV array from switching harmonics, a filter capacitor must be positioned at the input side of the boost converter. The necessary capacitance can be determined through the following equation:

$$C_{pv} = \frac{T\,\Delta i_{pv}}{8\,\Delta v_{pv}} \tag{12}$$

where T, Δipv and Δv_{pv} are switching period, minimum current and voltage ripple, respectively.

B. Boost Inductor:

The value of boost inductor is selected based on the allowable peak-to-peak inductor-current ripple. The required inductance is determined by the input voltage v_{pv}, duty ratio D, switching frequency f_s, and allowable current ripple Δi_{pv}. Therefore, the boost inductance is calculated using the following equation.

$$L_b = \frac{v_{pv} D(1-D)}{2\Delta i_{pv} f_s} \tag{13}$$

C. DC-link Capacitor:

The DC-link capacitor is designed to maintain an acceptable output voltage with a THD below 5% under the considered loading conditions. The maximum load condition represents the most demanding operating case for the DC-link capacitor design. As the loading condition changes, the amplitude of the ripple at twice the power-line frequency in the DC-link voltage also varies, which can slightly affect the magnitude of this ripple propagated back to the PV array. Therefore the DC-link capacitance of a single-phase inverter is determined based on the allowable voltage ripple across the capacitor [24], as given by:

$$C_{dc} = \frac{p_{pv}}{\omega_g \Delta v_{dc} v_{dc}} \tag{14}$$

where p_{pv}, ω_g and Δv_{dc} are the nominal PV power, grid frequency and minimum voltage ripple in DC-link.

D. Flying Capacitor (C_{fc}):

The flying capacitor is designed to maintain the required capacitor voltage while limiting its voltage ripple during switching operation. In the design, the switching-period voltage ripple is assumed to be negligible compared with the overall capacitor-voltage variation. Accordingly, the flying capacitor is designed using the following expression [20], [37].

$$C_{fc} = \frac{\int_0^{\pi} I_{o,m} sin(\omega t) d(t) d(\omega t)}{\Delta v_{fc}}. \tag{15}$$

where $I_{o,m}$ is the peak value of rated load current, Δv_{fc} is the allowable voltage ripple of a flying capacitor.

E. Filter Inductance:

The design constraints governing the selection of the filter components are discussed in [37]. The inductor value is mainly determined by the allowable output-current ripple, and its expression for the HM scheme is given by

$$L_f > \frac{v_{pv}}{4\Delta I_{max} f_s}. \tag{16}$$

where v_{pv}, f_s, and ΔI_{max} are the PV voltage, switching frequency and maximum current ripple respectively.

V. Results and Discussion

A. Simulation Results

Table VI presents the simulation parameters chosen for the proposed 1 kW two-stage system. The performance comparison of the proposed system is assessed through numerical simulations of various control strategies including P&O-DQ, P&O-OCC, RCC-DQ, and RCC-OCC using MATLAB/Simulink. Fig. 9 presents the transient responses of PV power, grid voltage, and grid current during the step change in solar irradiation from 600 W/m^2 to 1000 W/m^2.These responses depict how each control strategy performs dynamically when there is a sudden increase in solar irradiance, reflecting the system's ability to adapt quickly and maintain stable operation during such transient conditions. Fig. 10 depicts the steady-state characteristics of the system, showing

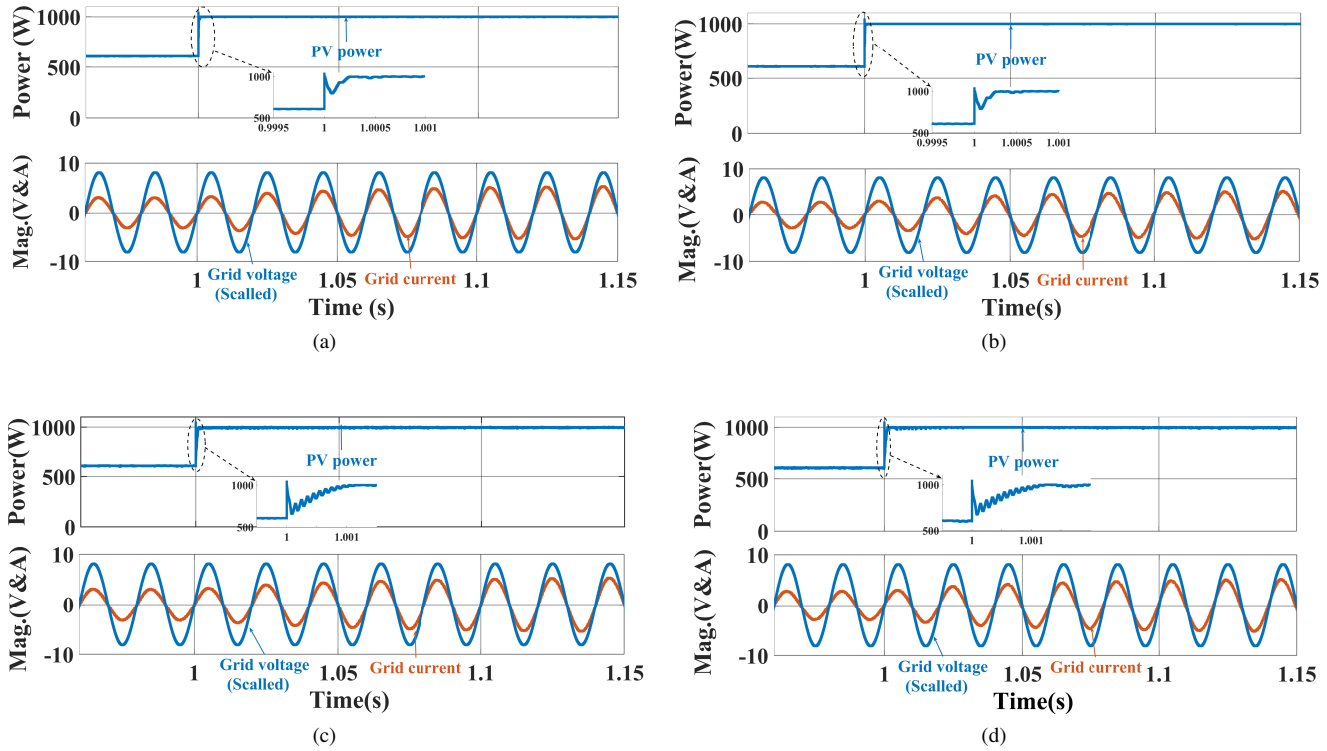

Fig. 9. Simulation waveforms during transient state. (a) P&O and DQ. (b) P&O and OCC. (c) RCC and DQ. (d) RCC and OCC.

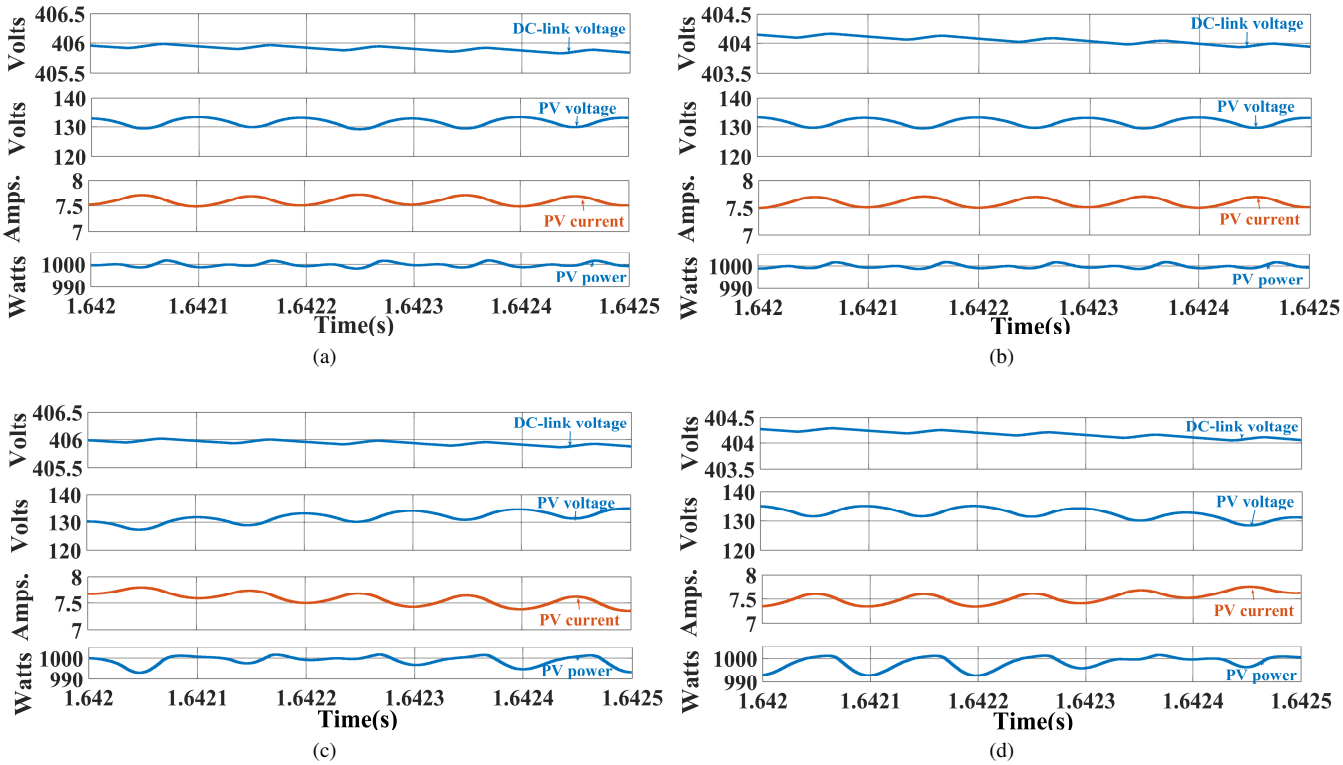

Fig. 10. Simulation waveforms during steady state. (a) P&O and DQ. (b) P&O and OCC. (c) RCC and DQ. (d) RCC and OCC.

the behavior of PV voltage, PV current, and PV power under stable operating conditions. It is observed that the transient and steady-state performance of the proposed RCC MPPT closely replicates that of the conventional P&O methods, while offering the advantage of a simpler and less complex design. Fig. 11 presents the grid voltage and current waveforms during steady-state operation for all control strategies under consideration. The results indicate that the grid synchronization achieved using the OCC method effectively replicates the performance of the conventional DQ control, but without requiring a grid voltage sensor.

TABLE VI
SYSTEM PARAMETERS AND OPERATING CONDITIONS USED IN THE SIMULATION AND HARDWARE-IN-THE-LOOP EXPERIMENTS

Parameter	Value	Parameter	Value
Power rating (P)	1 kW	Voltage at MPP (V_{mpp})	132 V
Current at MPP (I_{mpp})	7.61 A	DC-link voltage (V_{dc})	400 V
Output voltage (V_{rms})	230 V	Switching frequency (f_s)	10 kHz
Power frequency (f)	50 Hz	Boost inductor (L_b)	5.85 mH
PV-side capacitor (C_{pv})	5.5 μF	Flying capacitor (C_{fc})	1100 μF
DC-link capacitor (C_{dc})	1500 μF	Diode bridge rectifier load	8.5 Ω, 180 mH
k_p,k_i (both P&O and RCC)	0.015 and 15	k_p,k_i (both dq and OCC)	0.17 and 0.4

Furthermore, to validate the robustness of the proposed system under non-ideal operating conditions, its performance is evaluated in the presence of local nonlinear loads, irradiance variations, and grid-frequency deviations. Specifically, a local nonlinear load comprising a diode bridge rectifier feeding an RL circuit is connected along with a grid impedance of 0.08 + j0.534 Ω. This configuration introduces a distorted voltage at the PCC with a Total Harmonic Distortion (THD) of 4.85%, which is close to the maximum permissible voltage distortion limit of 5% specified by IEEE 519-2022. The corresponding simulation results obtained for the proposed system under these conditions are presented in Figs. 12 and 13. Figs. 12(a)-(c) demonstrate that the introduced nonlinearities have a negligible effect on the transient and steady-state performance of the proposed system. Furthermore, Fig. 12(d) shows that the proposed RCC-based MPPT effectively tracks the available PV power with a response time of less than 50 ms during rapid changes in irradiance. Similarly, Fig. 13 illustrates the steady-state performance of the proposed system under different grid-frequency conditions, demonstrating effective grid synchronisation and stable operation over the considered frequency range. Fig. 14 depicts the performance of the proposed control strategy under the influence of measurement noise. The system is simulated under two irradiance conditions, namely, 1000 W/m^2 and 300 W/m^2, with measurement noise added to the sensing signals. It is observed from Figs. 14(a) and (b) that the influence of measurement noise on the tracking performance of the proposed system is considerably low. The variation in the active power tracking is limited to 5–10 W only. Moreover, the proposed control method achieves the lowest grid-current THD of 3.44% among the considered cases, as presented in Table VII, and fully complies with the requirements specified in the IEEE 1547 standard.

In addition, a comprehensive performance analysis of the proposed system is carried out using the steady-state and transient metrics presented in Table VIII, including PV voltage ripple, PV current ripple, PV power ripple, power loss, transient response time, and energy loss. The results in Table VIII provide insight into the overall energy yield of the PV array. During transient conditions, the RCC-based MPPT scheme exhibits slightly higher energy loss due to its comparatively longer response time. However, this is compensated by its lower steady-state power loss, as the PV system operates predominantly under steady-state conditions. In particular, the proposed RCC-OCC strategy reduces the steady-state power loss by approximately 0.39 W compared with the conventional P&O-DQ scheme and exhibits lower steady-state power ripple, indicating reduced oscillations around the MPP. Consequently, the proposed RCC-based MPPT provides improved overall energy-harvesting performance despite its slightly slower transient response. Therefore, the proposed control strategy offers a cost-effective solution for single-phase two-stage PV systems while maintaining performance comparable to conventional approaches. To further validate the proposed system, experimental and hardware-in-the-loop implementation and testing are carried out, as presented in the following sections.

TABLE VII
SUMMARY OF THD VALUES FF GRID CURRENT

	Case 1	Case 2	Case 3	Case 4
THD of i_g	4.5%	4.33%	4.55%	3.44%

TABLE VIII
PERFORMANCE COMPARISON OF THE PROPOSED TOPOLOGY WITH OTHER CONSIDERED TOPOLOGIES

Case	MPPT	Inverter control	Steady-state performance				Transient performance	
			Ripple in v_{pv} (V)	Ripple in i_{pv} (A)	Ripple in p_{pv} (W)	Power loss (W)	Transient time (s)	Energy loss (J)
Case 1	P&O	DQ	3.972	0.1246	3.62	1.92	0.3	2.2
Case 2	P&O	OCC	4.0	0.18	3.429	1.92	0.3	1.7
Case 3	RCC	DQ	3.824	0.1271	2.815	1.53	0.5	3.7
Case 4	RCC	OCC	3.851	0.1279	3.06	1.53	0.5	2.4

B. Experimental Validation

The practical implementation of the proposed RCC MPPT is experimentally verified using an experimental test bench in the laboratory, as shown in Fig.15. The experimental test bench includes a PV emulator to emulate the required PV characteristics, with the soft panel installed on the host PC. A DC–DC converter and an inverter implemented using Semikron switches are used as the first and second stages of the system, respectively. The inverter in the experimental setup is an H-bridge inverter. However, the implemented experimental system reproduces the essential RCC functionality, thereby enabling experimental verification of the proposed RCC-based MPPT operation. The proposed RCC-based MPPT and OCC control schemes are implemented using TMS320F28379D DSP controller boards. Fig. 16 illustrates the results obtained from the experimental test bench utilizing the parameters detailed in Table IX. Fig. 16(a) depicts the MPP test results obtained from the soft panel interface of the PV emulator. It can be observed from the MPP test results obtained using

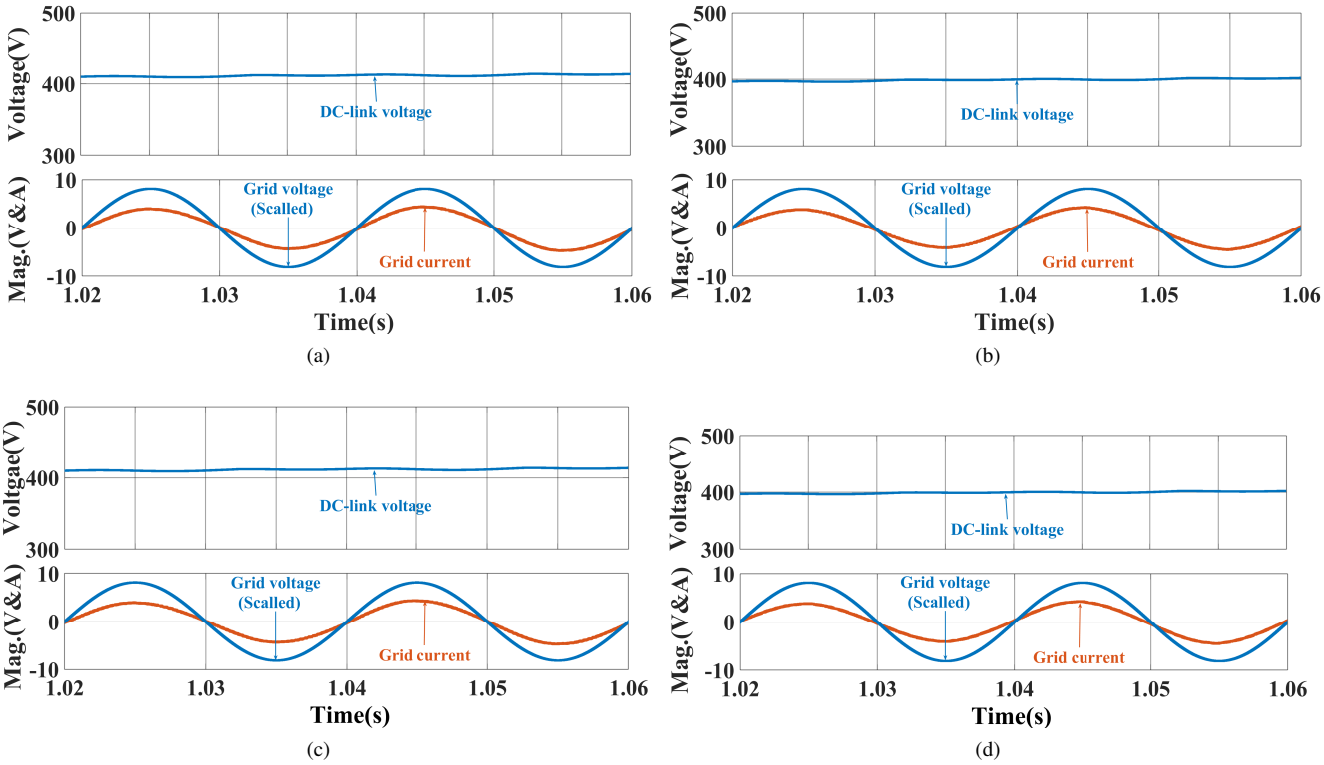

Fig. 11. Simulation waveforms during steady state. (a) P&O and DQ. (b) P&O and OCC. (c) RCC and DQ. (d) RCC and OCC.

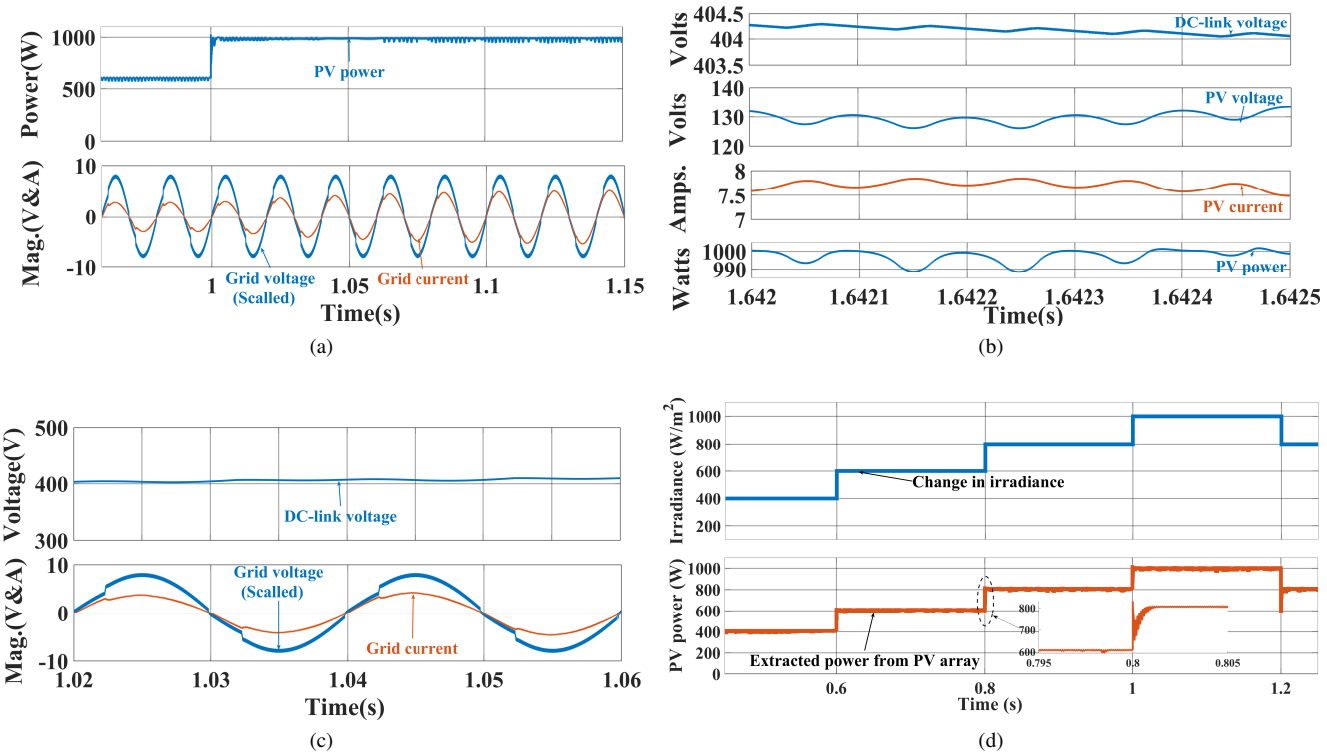

Fig. 12. Simulation waveforms of the proposed system under nonlinear load conditions: (a) transient response; (b)–(c) steady-state performance; and (d) response to rapid irradiance changes.

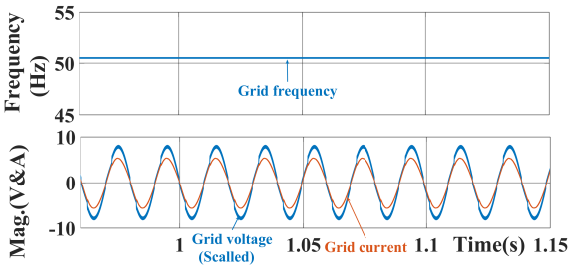

(a)

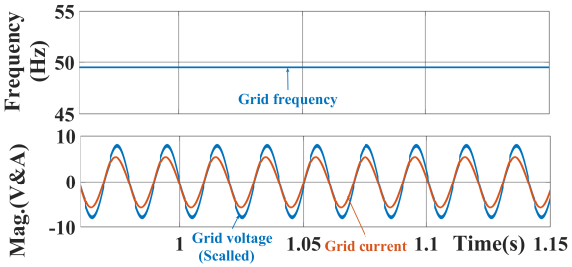

(b)

Fig. 13. Simulation waveforms of the proposed system under different grid-frequency conditions: (a) grid frequency of 50.5 Hz; and (b) grid frequency of 49.5 Hz.

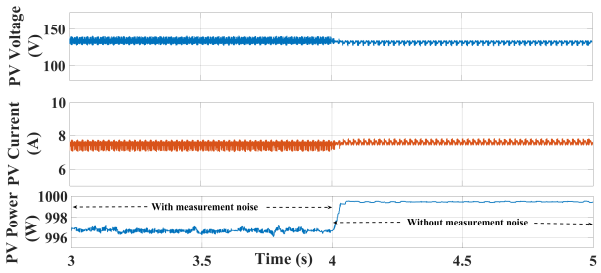

(a)

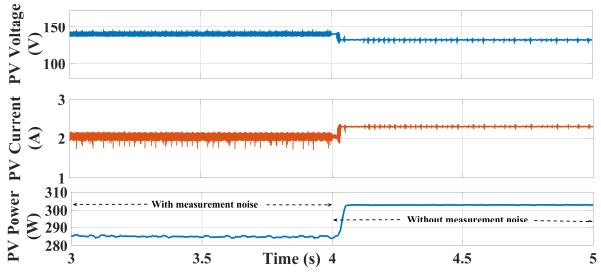

(b)

Fig. 14. Simulation waveforms of the proposed system under the influence of measurement noise: (a) Maximum irradience (1000 W/m2) ; and (b) Low irradiance(300 W/m2).

the soft panel that the proposed RCC MPPT achieves a tracking efficiency of 98.12%. Similarly, Fig. 16(b) shows the experimental waveforms of the PV voltage, PV current, and PV power at the switching-frequency time scale, further confirming the effective operation of the proposed RCC MPPT under steady-state conditions. The experimental waveforms of the grid voltage and current during steady-state operation, shown in Fig. 16, demonstrate the effective synchronization capability of the OCC control scheme with the utility grid without requiring a PLL or grid-voltage sensor.

TABLE IX
KEY SYSTEM PARAMETERS AND EXPERIMENTAL SETTINGS FOR VALIDATION OF THE PROPOSED TOPOLOGY

Parameter	Value	Parameter	Value
Power rating (P)	1 kW	Voltage at MPP (V_{mpp})	150 V
Current at MPP (I_{mpp})	6.7 A	DC-link voltage (V_{dc})	400 V
Output voltage (V_{rms})	230 V	Switching frequency (f_s)	10 kHz
Power frequency (f)	50 Hz	Boost inductor (L_b)	6 mH

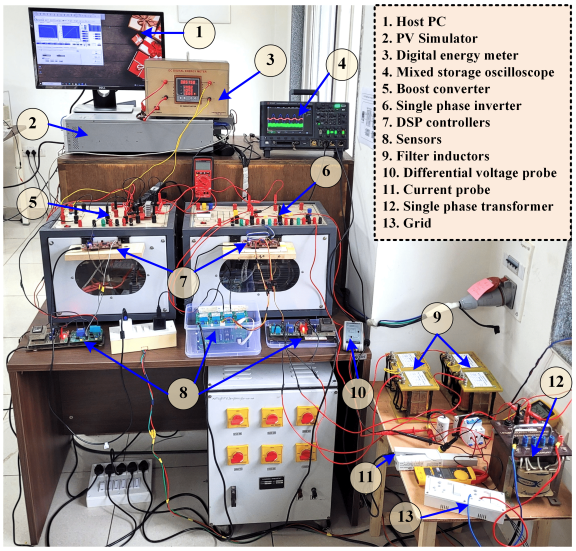

Fig. 15. Experimental test bench of 1 kW two-stage single phase grid tied PV system.

C. Hardware-in-loop (HIL) Experimental Validation

Since the experimental validation uses an H-bridge inverter configuration, a HIL experimental setup is used in this section to evaluate the performance of the proposed system under the considered control strategies. In this setup, a real-time digital simulator (RTDS OP4500) is used to emulate the power circuit, which employs a Type-I common-ground inverter, while the MPPT algorithm and associated control functions are executed on a Texas Instruments TMS320F28335 DSP board through a host PC. The overall HIL experimental setup is illustrated in Fig. 17. The parameters used for the HIL testing are listed in Table VI and are the same as those employed for the MATLAB simulations. The resulting outputs of the proposed system for the considered control strategies are presented in Fig. 18–20. Fig. 18 illustrates the transient response of the system under the considered control strategies for a step change in irradiance from 600 W/m^2 to 1000 W/m^2. Similarly, Figs. 19 and 20 show the steady-state responses under ideal operating conditions of the system. Furthermore, HIL testing is also carried out under grid-voltage distortion,

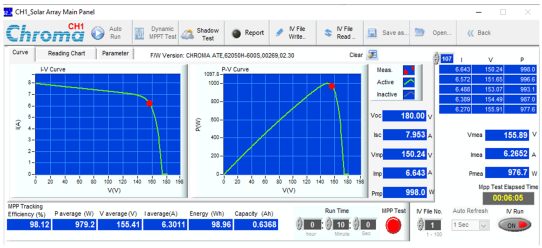

(a)

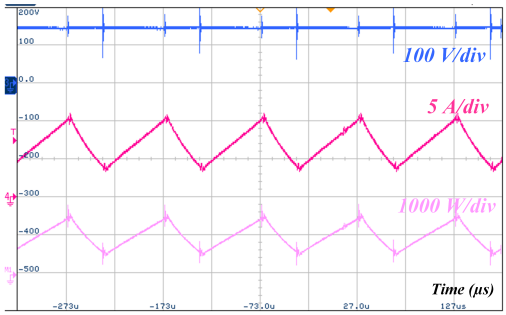

(b)

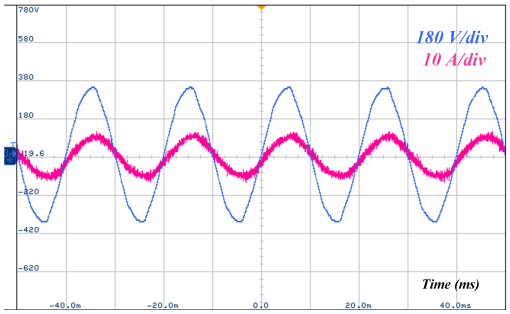

(c)

Fig. 16. Experimental waveforms of the proposed system (a) MPPT test from soft panel interface (b) TR1: PV voltage, TR2: PV current and TR3: PV power (c) Grid voltage and current.

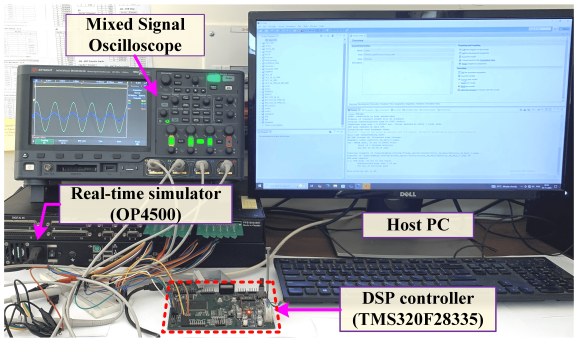

Fig. 17. HIL experimental setup.

grid-frequency deviations, and changes in irradiance, which are considered in the simulation. Fig. 21 presents the performance of the proposed system under grid voltage distortion, grid-frequency deviations, and rapid irradiance variations . It is evident from Figs. 21(a), (b), and (c) that the proposed control strategy effectively maintains grid synchronization under grid-voltage distortion and grid-frequency variations. Fig. 21(d) reveals that the proposed MPPT successfully tracks the available power within its response time during rapid changes in irradiance. The results indicate that the HIL experimental results closely aligns with the simulation results presented in section V-A. To highlight the advantages of the proposed scheme, it is compared with other topologies considered in this study, as summarized in Table X. The comparison is based on key design and implementation criteria, including the requirements for grid voltage and current sensors, the use of a PLL, sensitivity to external perturbations, and the resulting system complexity and cost. From the comparison, it can be observed that conventional approaches such as P&O with DQ control and RCC with DQ control require both voltage and current sensors as well as a PLL, resulting in increased system complexity and cost. Although the P&O with OCC method reduces the dependence on sensors and eliminates the PLL, it remains sensitive to external disturbances. In contrast, the proposed RCC with OCC topology removes the need for a grid voltage sensor and PLL, demonstrates robustness against external perturbations, and achieves the lowest overall complexity and cost among the compared methods.

TABLE X
COMPARISON OF THE PROPOSED TOPOLOGY WITH OTHER CONSIDERED TOPOLOGIES

Topology	Grid Voltage Sensor	Grid Current Sensor	PLL	External Perturbations	Complexity and Cost
P&O + DQ	✓	✓	✓	×	High
P&O + OCC	×	✓	×	✓	Moderate
RCC + DQ	✓	✓	✓	×	High
RCC + OCC	×	✓	×	×	Low

From the comprehensive design, analysis using simulation and HIL, and experimental hardware validation. The major contributions of this work are as follows:

- The RCC MPPT, which effectively utilizes the twice-the-line-frequency ripple in single-stage systems, is investigated for the first time in a two-stage system, where the ripple is back-propagated to the PV array with a lower magnitude.
- An average model is developed to determine the amount of 100-Hz ripple back-propagated from the DC-link capacitor to the PV array, thereby providing a theoretical basis for understanding the operational limits of the RCC algorithm.
- The proposed RCC implementation employs low-pass filters and avoids derivative-based computations, thereby reducing sensitivity to measurement noise and ensuring reliable MPP tracking performance under noisy operating conditions.
- The proposed system integrates PLL-less grid synchronization through OCC control, constant common-mode voltage operation using the Type-I common-ground inverter, and a modulation strategy that reduces the requirement for high-frequency switching devices.
- Simulation, HIL, and experimental results are presented to validate the proposed approach and demonstrate effective MPPT and grid-integration performance under different operating conditions.

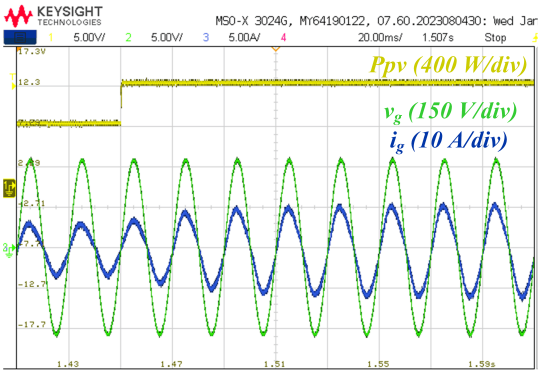

(a)

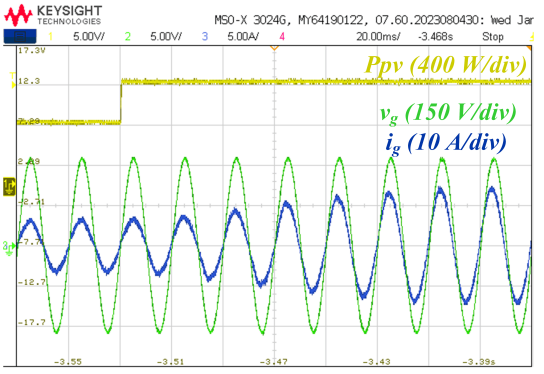

(b)

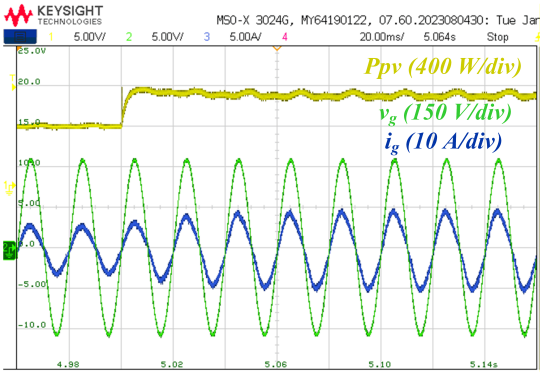

(c)

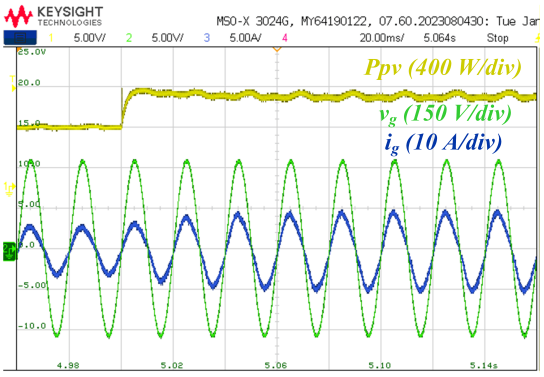

(d)

Fig. 18. HIL experimental results during transient state. (TR:1) PV power(400 W/div). (TR:2) Grid voltage(150 V/div) and Grid current(10 A/div). (a) P&O and DQ. (b) P&O and OCC. (c) RCC and DQ. (d) RCC and OCC.

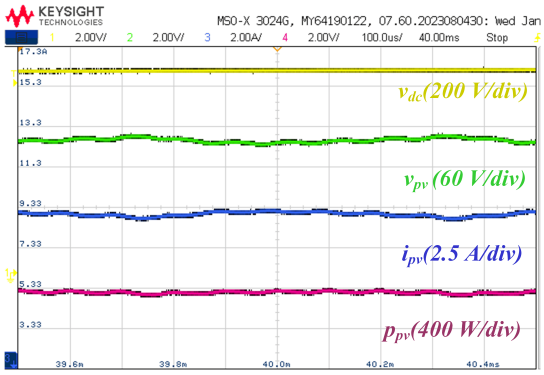

(a)

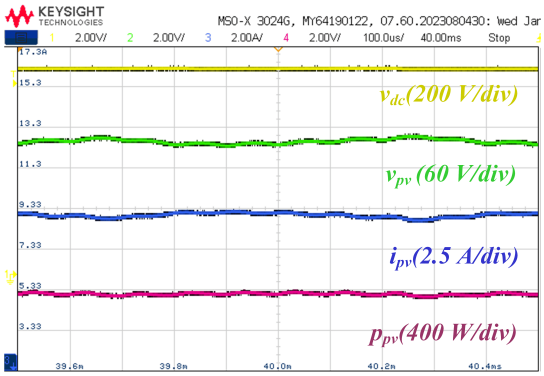

(b)

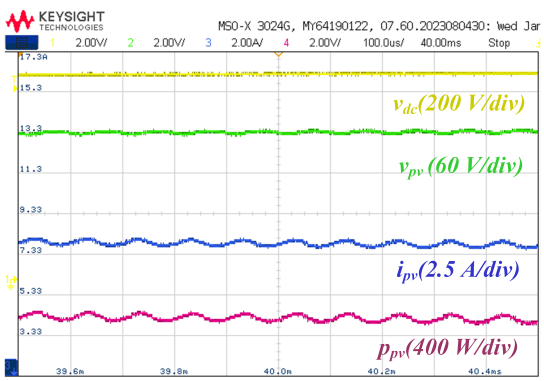

(c)

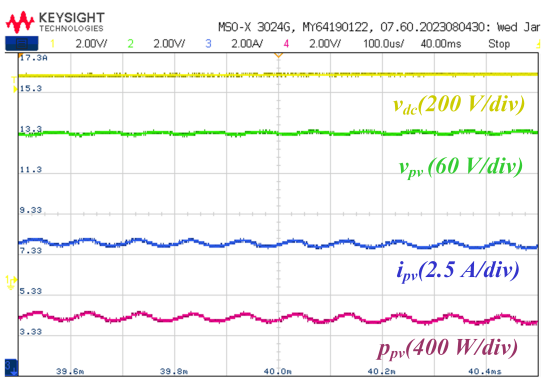

(d)

Fig. 19. HIL experimental results during steady state. (TR:1) DC link voltage(200v/div).(TR:2) PV voltage(60V/div). (TR:3). PV current(2.5A/div). (TR:4) PV power(400W/div) (a) P&O and DQ. (b) P&O and OCC. (c) RCC and DQ. (d) RCC and OCC.

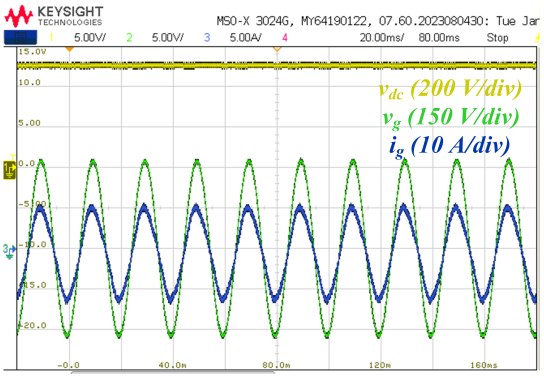

(a)

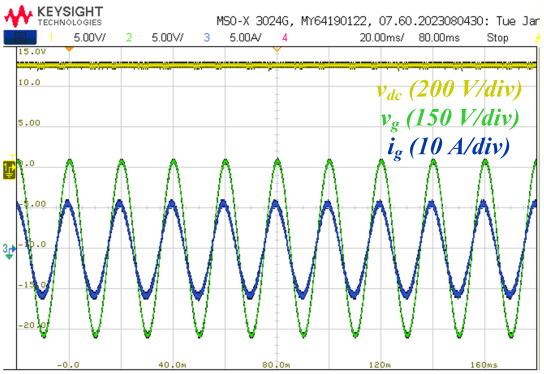

(b)

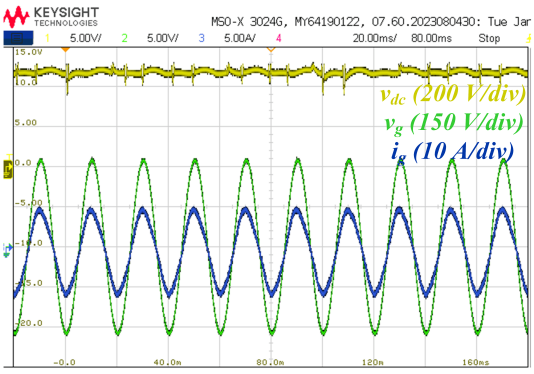

(c)

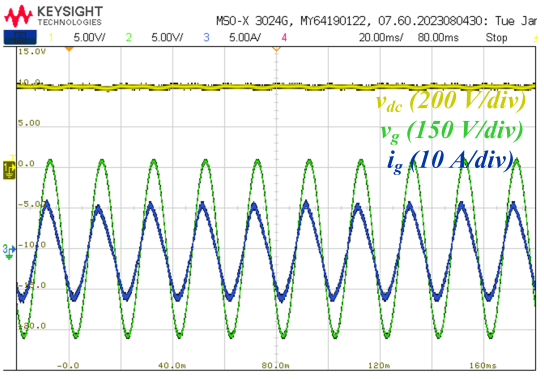

(d)

Fig. 20. HIL experimental results during steady state. (TR:1) DC link voltage(200 V/div). (TR:2) Grid voltage(150 V/div) and Grid current(10 A/div) (a) P&O and DQ. (b) P&O and OCC. (c) RCC and DQ. (d) RCC and OCC.

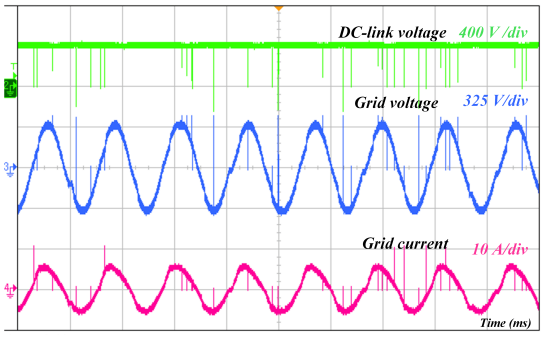

(a)

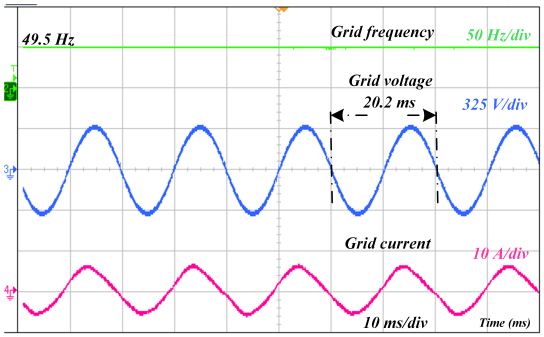

(b)

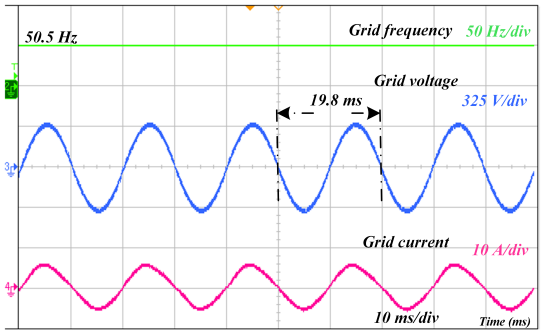

(c)

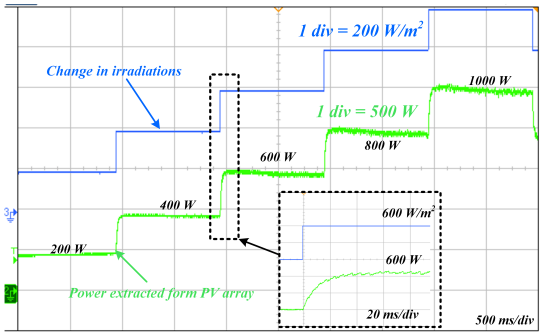

(d)

Fig. 21. HIL experimental results of the proposed system under (a) distorted grid voltage (b) a grid frequency of 49.5 Hz; (c) a grid frequency of 50.5 Hz; and (d) rapid changes in irradiance.

VI. Conclusion

This paper presented a simple and cost-effective design for a single-phase, two-stage grid-tied PV system intended for residential applications. An RCC-based MPPT technique was employed for the boost converter, which exploits the inherent

voltage and current ripple at twice the power-line frequency (100 Hz in 50 Hz systems) appearing across the capacitor connected in parallel with the PV array, thereby achieving maximum power point tracking without the need for external perturbations. The proposed system integrates the following features that have been individually investigated in the reported literature. A one-cycle control (OCC) technique enables effective grid synchronization and current control without the need for a phase-locked loop. The common-ground transformerless inverter is used for power conversion, maintaining a constant common-mode voltage and thus reducing leakage currents. Furthermore, the adopted inverter modulation strategy ensures that two switches are operating at the switching frequency, while the remaining two are operating at the power frequency, lowering the switching loss. The performance and effectiveness of the proposed system, in comparison with conventional approaches, are validated through MATLAB/Simulink simulations and further verified by hardware-in-the-loop testing using a digital signal processor-based controller. The proposed control strategy is also experimentally validated using an experimental test bench. The results demonstrate that the RCC–OCC scheme achieves a tracking efficiency of 98.12% while ensuring effective grid synchronization without requiring a PLL and grid-voltage sensor. Overall, the proposed approach achieves performance comparable to conventional control methods while offering reduced design complexity and lower implementation cost.

REFERENCES

[1] R. Panigrahi, S. K. Mishra, S. C. Srivastava, A. K. Srivastava, and N. N. Schulz, "Grid integration of small-scale photovoltaic systems in secondary distribution network - a review," *IEEE Transactions on Industry Applications*, vol. 56, no. 3, pp. 3178–3195, 2020, doi:10.1109/TIA.2020.2979789.

[2] D. Boruah and S. Singh Chandel, "A comprehensive analysis of eight rooftop grid-connected solar photovoltaic power plants with battery energy storage for enhanced energy security and grid resiliency," *Solar Energy*, vol. 266, p. 112154, 2023, doi:10.1016/j.solener.2023.112154.

[3] M. Morey, N. Gupta, M. M. Garg, and A. Kumar, "A comprehensive review of grid-connected solar photovoltaic system: Architecture, control, and ancillary services," *Renewable Energy Focus*, vol. 45, pp. 307–330, 2023, doi:10.1016/j.ref.2023.04.009.

[4] A. K. Yadav, H. Malik, S. M. S. Hussain, and T. S. Ustun, "Case study of grid-connected photovoltaic power system installed at monthly optimum tilt angles for different climatic zones in india," *IEEE Access*, vol. 9, pp. 60 077–60 088, 2021, doi:10.1109/ACCESS.2021.3073136.

[5] B. Guo, M. Su, Y. Sun, H. Wang, B. Liu, X. Zhang, J. Pou, Y. Yang, and P. Davari, "Optimization design and control of single-stage single-phase pv inverters for mppt improvement," *IEEE Transactions on Power Electronics*, vol. 35, no. 12, pp. 13 000–13 016, 2020, doi:10.1109/TPEL.2020.2990923.

[6] B. Subudhi and R. Pradhan, "A comparative study on maximum power point tracking techniques for photovoltaic power systems," *IEEE Transactions on Sustainable Energy*, vol. 4, no. 1, pp. 89–98, 2013, doi:10.1109/TSTE.2012.2202294.

[7] K. Y. Yap, C. R. Sarimuthu, and J. M.-Y. Lim, "Artificial intelligence based mppt techniques for solar power system: A review," *Journal of Modern Power Systems and Clean Energy*, vol. 8, no. 6, pp. 1043–1059, 2020, doi:10.35833/MPCE.2020.000159.

[8] L. E. Hernandez Aguilar, G. Vazquez Guzman, P. R. Martinez Rodriguez, and D. Aztatzi Pluma, "Design and validation of a hybrid mppt algorithm for pvs using an interleaved boost converter," *IEEE Latin America Transactions*, vol. 23, no. 10, pp. 901–909, 2025, doi:10.1109/TLA.2025.11150626.

[9] T. M. de Lima and J. A. C. B. Oliveira, "Fpga-based fuzzy logic controllers applied to the mppt of pv panels—a systematic review," *IEEE Transactions on Fuzzy Systems*, vol. 32, no. 8, pp. 4260–4269, 2024, doi:10.1109/TFUZZ.2024.3392846.

[10] T. Esram, J. Kimball, P. Krein, P. Chapman, and P. Midya, "Dynamic maximum power point tracking of photovoltaic arrays using ripple correlation control," *IEEE Transactions on Power Electronics*, vol. 21, no. 5, pp. 1282–1291, 2006, doi:10.1109/TPEL.2006.880242.

[11] C. Barth and R. C. N. Pilawa-Podgurski, "Dithering digital ripple correlation control for photovoltaic maximum power point tracking," *IEEE Transactions on Power Electronics*, vol. 30, no. 8, pp. 4548–4559, 2015, doi:10.1109/TPEL.2014.2357796.

[12] J. M. Sosa, P. R. Martinez-Rodriguez, G. Escobar, G. Vazquez, A. A. Valdez-Fernandez, and J. F. Martinez-Garcia, "Analysis and validation for an inverter-side current controller in lcl grid-connected power systems," *Journal of Modern Power Systems and Clean Energy*, vol. 8, no. 2, pp. 387–398, 2020, doi:10.35833/MPCE.2018.000505.

[13] N. Koshkarbay, K. K. Mohammed, S. Mekhilef, N. Kuttybay, A. Saymbetov, M. Nurgaliyev, and N. Kalassov, "High efficiency hybrid mppt technique with integrated partial shading detection for photovoltaic systems under varying shading conditions," *Renewable Energy*, vol. 261, p. 125244, 2026, doi:10.1016/j.renene.2026.125244.

[14] A.-M. Badea, D. Manaila-Maximean, L. Fara, and D. Craciunescu, "Maximizing solar photovoltaic energy efficiency: Mppt techniques investigation based on shading effects," *Solar Energy*, vol. 285, p. 113082, 2025, doi:10.1016/j.solener.2024.113082.

[15] J. Ahmed and Z. Salam, "A modified p&o maximum power point tracking method with reduced steady-state oscillation and improved tracking efficiency," *IEEE Transactions on Sustainable Energy*, vol. 7, no. 4, pp. 1506–1515, 2016, doi:10.1109/TSTE.2016.2568043.

[16] D. Casadei, G. Grandi, and C. Rossi, "Single-phase single-stage photovoltaic generation system based on a ripple correlation control maximum power point tracking," *IEEE Transactions on Energy Conversion*, vol. 21, no. 2, pp. 562–568, 2006, doi:10.1109/TEC.2005.853784.

[17] V. R. Reddy and E. S. Sreeraj, "Integration of ripple correlation mppt technique with one-cycle-controlled transformerless inverter for single-phase single-stage photovoltaic systems," in *IECON 2017 - 43rd Annual Conference of the IEEE Industrial Electronics Society*, 2017, pp. 2552–2557, doi:10.1109/IECON.2017.8216429.

[18] W. Li, Y. Gu, H. Luo, W. Cui, X. He, and C. Xia, "Topology review and derivation methodology of single-phase transformerless photovoltaic inverters for leakage current suppression," *IEEE Transactions on Industrial Electronics*, vol. 62, no. 7, pp. 4537–4551, 2015, doi:10.1109/TIE.2015.2399278.

[19] M. N. H. Khan, M. Forouzesh, Y. P. Siwakoti, L. Li, T. Kerekes, and F. Blaabjerg, "Transformerless inverter topologies for single-phase photovoltaic systems: A comparative review," *IEEE Journal of Emerging and Selected Topics in Power Electronics*, vol. 8, no. 1, pp. 805–835, 2020, doi:10.1109/JESTPE.2019.2908672.

[20] Y. P. Siwakoti and F. Blaabjerg, "Common-ground-type transformerless inverters for single-phase solar photovoltaic systems," *IEEE Transactions on Industrial Electronics*, vol. 65, no. 3, pp. 2100–2111, 2018, doi:10.1109/TIE.2017.2740821.

[21] A. Kadam and A. Shukla, "A multilevel transformerless inverter employing ground connection between pv negative terminal and grid neutral point," *IEEE Transactions on Industrial Electronics*, vol. 64, no. 11, pp. 8897–8907, 2017, doi:10.1109/TIE.2017.2696460.

[22] D. Ertekin, "An fpga-based switching photovoltaic-connected inverter topology for leakage current suppression in grid-connected utilizations," *International Journal of Circuit Theory and Applications*, vol. 48, no. 10, pp. 1724–1743, 2020, doi:10.1002/cta.2844.

[23] A. H. Sabry, Z. M. Mohammed, F. H. Nordin, N. H. Nik Ali, and A. S. Al-Ogaili, "Single-phase grid-tied transformerless inverter of zero leakage current for pv system," *IEEE Access*, vol. 8, pp. 4361–4371, 2020, doi:10.1109/ACCESS.2019.2963284.

[24] A. R. Gautam, D. M. Fulwani, R. R. Makineni, A. K. Rathore, and D. Singh, "Control strategies and power decoupling topologies to mitigate 2ω-ripple in single-phase inverters: A review and open challenges," *IEEE Access*, vol. 8, pp. 147 533–147 559, 2020, doi:10.1109/ACCESS.2020.3015315.

[25] S. G. Jorge, J. A. Solsona, and C. A. Busada, "Nonlinear control of a two-stage single-phase dc-ac converter," *IEEE Journal of Emerging and Selected Topics in Industrial Electronics*, vol. 3, no. 4, pp. 1038–1045, 2022, doi:10.1109/JESTIE.2022.3151003.

[26] A. Kumar, A. Prajapati, N. Kumar, and J. Dhayal, "Single-phase two-stage grid integrated solar pv system with oso-ai control and pspo mppt,"

IEEE Transactions on Industry Applications, vol. 61, no. 6, pp. 9662–9670, 2025, doi:10.1109/TIA.2025.3584292.

[27] R. K. Jain, B. V. Reddy, and G. H. K. Varma, "Robust and efficient control strategy for single-phase two-stage pv grid-tied system with improved power quality," *Renewable Energy Focus*, vol. 48, p. 100524, 2024, https://doi.org/10.1016/j.ref.2023.100524. [Online]. Available: https://www.sciencedirect.com/science/article/pii/S1755008423001205

[28] N. Femia, M. Fortunato, G. Petrone, G. Spagnuolo, and M. Vitelli, "Dynamic model of a grid-connected photovoltaic inverter with one cycle control," in *2009 35th Annual Conference of IEEE Industrial Electronics*, 2009, pp. 4561–4565, doi:10.1109/IECON.2009.5414867.

[29] E. S. Sreeraj, K. Chatterjee, and S. Bandyopadhyay, "One-cycle-controlled single-stage single-phase voltage-sensorless grid-connected pv system," *IEEE Transactions on Industrial Electronics*, vol. 60, no. 3, pp. 1216–1224, 2013, doi:10.1109/TIE.2012.2191755.

[30] V. R. Reddy and E. S. Sreeraj, "A hybrid islanding detection method for one cycle controlled pv inverter system," *IEEE Journal of Emerging and Selected Topics in Industrial Electronics*, vol. 3, no. 3, pp. 777–787, 2022, doi:10.1109/JESTIE.2021.3099395.

[31] S. Chakraborty, K. Sarkar, D. Maiti, A. Chakrabarti, S. Dasgupta, and S. K. Biswas, "A single-phase grid-tied transformer-less multilevel solar inverter with voltage boost," *IEEE Transactions on Industrial Electronics*, vol. 73, no. 1, pp. 379–389, 2026, doi:10.1109/TIE.2025.3589430.

[32] M. Salimi, F. Radmand, and M. H. Firouz, "Dynamic modeling and closed-loop control of hybrid grid-connected renewable energy system with multi-input multi-output controller," *Journal of Modern Power Systems and Clean Energy*, vol. 9, no. 1, pp. 94–103, 2021, doi:10.35833/MPCE.2018.000353.

[33] R. Bisht, R. Bhattarai, S. Subramaniam, and S. Kamalasadan, "A novel synchronously rotating reference frame based adaptive control architecture for enhanced grid support functions of single-phase inverters," *IEEE Transactions on Industry Applications*, vol. 56, no. 4, pp. 4288–4298, 2020, doi:10.1109/TIA.2020.2994879.

[34] C.-Y. Tang and J.-H. Jheng, "An active power ripple mitigation strategy for three-phase grid-tied inverters under unbalanced grid voltages," *IEEE Transactions on Power Electronics*, vol. 38, no. 1, pp. 27–33, 2023, doi:10.1109/TPEL.2022.3198410.

[35] N. F. Ibrahim, K. Mahmoud, M. Lehtonen, and M. M. F. Darwish, "Comparative analysis of three-phase pv grid connected inverter current control schemes in unbalanced grid conditions," *IEEE Access*, vol. 11, pp. 42 204–42 221, 2023, doi:10.1109/ACCESS.2023.3270262.

[36] J. Xu, J. Zhong, J. Kang, W. Dong, and S. Xie, "Stability analysis and robust parameter design of dc-voltage loop for three-phase grid-connected pv inverter under weak grid condition," *IEEE Transactions on Industrial Electronics*, vol. 71, no. 4, pp. 3776–3787, 2024, doi:10.1109/TIE.2023.3277020.

[37] L. Sreekumar, A. Shivanand Shirodkar, and S. ES, "Improved modulation methods for single-phase common-ground type transformerless inverter," in *2022 IEEE International Conference on Power Electronics, Drives and Energy Systems (PEDES)*, 2022, pp. 1–6, doi:10.1109/PEDES56012.2022.10080866.

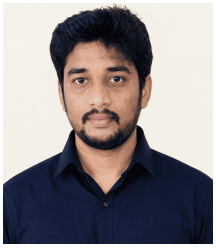

Raghavendra Bandaru received the B.Tech. degree in electrical and electronics engineering from Prakasam Engineering College, Kandukur, in 2012, and the M.E. degree in Electrical Engineering from Sir C R Reddy College of Engineering, Andhra Pradesh, in 2015. He is currently pursuing the Ph.D. degree in electrical and electronics engineering at the National Institute of Technology Goa. His research interests include grid integration of renewable-energy systems, power electronic converters, and grid-forming inverters.



Sreeraj E. S. received the B.Tech. degree in electrical and electronics engineering from the Regional Engineering College, Calicut, India, in 2001, and the M.Tech. degree in energy system engineering and the Ph.D. degree in electrical engineering from the Indian Institute of Technology Bombay, Mumbai, India, in 2006 and 2013, respectively. He was a Research Associate with The Energy and Research Institute, New Delhi, India, from 2006 to 2007 and worked as an Assistant Professor with the Birla Institute of Technology and Science, Pilani, India, from 2013 to 2014. Since 2014, he has been working as an Assistant Professor with Department of Electrical and Electronics Engineering, National Institute of Technology Goa, Veroda, India. His current research interests are renewable energy system modeling and power electronic converters.



Punnet Kuamr Goel received the B.Tech. degree in electrical engineering from IIT-Kanpur, Kanpur, India in 1987, the M.Tech. degree in power apparatus and systems from IIT-Delhi, New Delhi, India in 1989, the M.S. degree in electrical engineering from U.S.C., Los Angeles, Los Angeles, CA, USA in 2001, and the Ph.D. degree in electrical engineering from IIT-Delhi, India in 2009. In 1991, he joined Indian Administrative Service, where his assignments include Secretary (Power), Andaman & Nicobar Islands, India; Director (Thermal), Ministry of Power, Govt. of India; Executive Director, Rural Electrification Corporation of India Limited; Chairman and Managing Director, Delhi Transco and Secretary (Power), Govt. of NCT of Delhi, Commissioner, South Delhi Municipal Corporation, New Delhi; Principal Secretary (Power and Renewable Energy), Govt. of Goa; Secretary, Govt of india. Presently, he is with the Manipur State Power Company Limited (MSPCL), Manipur, India. His areas of interest include solar PV grid interface systems, renewable energy sources, microgrids, power electronics and electrical machines. Mr. Goel is the recipient of the National Energy Conservation Award from the President of India, in 2017.